



Comparison of Blade Resolved and Actuator Disk Simulations of a Ducted Wind Turbine

Junior E. Tchapdieu¹, Brian T. Helenbrook¹, and Kenneth D. Visser²

¹Mechanical and Aerospace Engineering Department, Clarkson University, Potsdam, NY 13699-5725, USA

Correspondence: Junior E. Tchapdieu (tchapdje@clarkson.edu)

Abstract. 3-D blade-resolved and 2-D actuator-disk simulations of a ducted wind turbine (DWT) were performed to investigate the fidelity of actuator disc predictions and the impact of 3-D effects on performance. Both simulations used Reynolds-averaged Navier-Stokes (RANS) equations with a $k-\epsilon$ turbulence model. The DWT had a five-bladed rotor with a GOE417a airfoil, and the duct utilized an E423 airfoil. The Reynolds number based on the diameter of the rotor was 1.24×10^6 . The design tip speed ratio was 2.9. The performance of the DWT from the blade-resolved simulation was 26% lower than the actuator disk simulation, with a significantly larger separation region inside the duct. These observations suggest that, while 2-D actuator disk simulations have a lower computational cost, predictions of the coefficient of power and flow separation may not be accurate. A possible reason is that the actuator disc model did not include swirl, which near the hub was observed to reach nearly 80% of the free stream velocity. Another possible reason is blade intermittency effects. The separation region on the duct increased as the blade passed and then reduced, but it was always larger than that in the actuator disk simulations.

1 Introduction

20

The presence of a duct around the rotor of a wind turbine increases the mass flow at the rotor and thus the power output of the device. As a result, ducted wind turbines (DWTs) have the potential to exceed the performance ceiling set by the Betz limit for open rotor turbines (ORTs). An extensive amount of work on ducted wind turbines has been performed both experimentally (Gilbert and Foreman, 1979; Kogan, et al., 1961; Gilbert et al., 1978; Gilbert and Foreman, 1983; Ohya et al., 2008; Ohya and Karasudani, 2010; Cresswell et al., 2015; Kanya and Visser, 2018) and analytically (Dick, 1986; Hansen et al., 2000; Van Bussel, 2025; Bontempo and Manna, 2014; Jamieson, 2008, 2009; Liu and Yoshida, 2015) to characterize the power enhancement. One of the most common tools used to predict the behavior of a ducted wind turbine is a 2-D actuator disk simulation.

2-D actuator disk simulations are a computationally cost-effective tool for DWT optimization. Using this approach, critical parameters such as the duct diameter, length, and horizontal position relative to the rotor can be analyzed (Abe and Ohya, 2004; Moeller and Visser, 2010; Venters et al., 2018). These parameters affect the area ratio between the rotor and the duct exit, which has a direct impact on performance (Foote and Agarwal, 2013). Notably, increasing the area ratio increases the flow velocity at the rotor plane and thus the power output. This implies that increasing the angle of attack of the duct will increase

²Department of Engineering Calvin University Grand Rapids, MI, USA 49546

https://doi.org/10.5194/wes-2025-207 Preprint. Discussion started: 20 October 2025

© Author(s) 2025. CC BY 4.0 License.





the power output. However, when a critical angle of attack is exceeded, the flow separates on the inner surface of the duct, reducing the effective exit area and leading to a decrease in power, as shown by Bagheri-Sadeghi et al. (2018). Their results demonstrate the value of 2-D actuator disk simulations in optimizing DWTs. For example, the ducted wind turbine analyzed in this study was designed using two-dimensional actuator disk simulations combined with blade element momentum theory for blade design (Visser, 2022).

Although 2-D actuator disk simulations are computationally efficient, they cannot capture details such as the influence of individual blades and the tip vortices they generate (Wang and Chen, 2008; Aranake et al., 2015). These limitations can be overcome by 3-D blade-resolved simulations. For example, Venters et al. (2018) noted that the stall angle of a duct is larger than that of an isolated airfoil due to the presence of the rotor, modeled as a disk. However, in real DWTs, the blades do not form a continuous disk, rather, it has been suggested that the tip vortices energize the boundary layer on the duct, delaying flow separation (Aranake et al., 2015). This implies that there may be significant differences between 2-D and 3-D results.

Studies have compared the behavior of 2-D and 3-D duct flows (Rahmatian et al., 2022), but none have included an actuator disk or a 3-D rotor in the simulations. Therefore, there is a lack of research on how the performance of DWTs designed using actuator disk simulations translates to blade-resolved simulations, and the literature lacks studies that compare the 2-D and 3-D flow fields. In particular, the accuracy of predicting the flow separation zone in the duct, one of the most critical design aspects of DWTs, remains unexplored.

This paper compares actuator disk and blade-resolved simulation methods for a DWT, and is structured as follows: Section 2 and section 3 present the blade-resolved and actuator-disk simulation setups, respectively. Section 4 then provides a comparison of the performance as predicted by the two approaches and section 5 presents comparisons of the 2-D and 3-D flow features.

2 Blade-Resolved Simulation Setup

45 This section validates the techniques used to obtain the blade-resolved numerical solutions and includes the definition of geometry, Fluent setup, mesh, and finally a study of grid convergence.

2.1 Geometry & Fluent Setup

The DWT analyzed in this study was five-bladed with a 3 m rotor diameter. Figure 1 shows front, lateral, and isometric views. Figure 1(a) and (b) illustrate that the DWT had the generator hub removed to decrease the computational complexity of the simulation. The operating conditions are given in Table 1, with a Reynolds number based on the diameter of the rotor of 1.24×10^6 .

The duct utilized an Eppler 423 (E423) airfoil for its cross-sectional profile, while the rotor blades utilized a GOE417a airfoil. Figure 2 shows the geometry of the two airfoils. Both the duct and blade airfoils were chosen for their high lift coefficients at lower Reynolds numbers (Selig et al., 1996). The blade airfoil was also selected for its ease of manufacturing (Schmitz, 1942). The chord length of the duct, c_{duct} , was 0.665 m and the chord length of the blade varied from 0.213 m at the root to 0.125 m

at the tip. The tip chord is defined as c_{blade} .





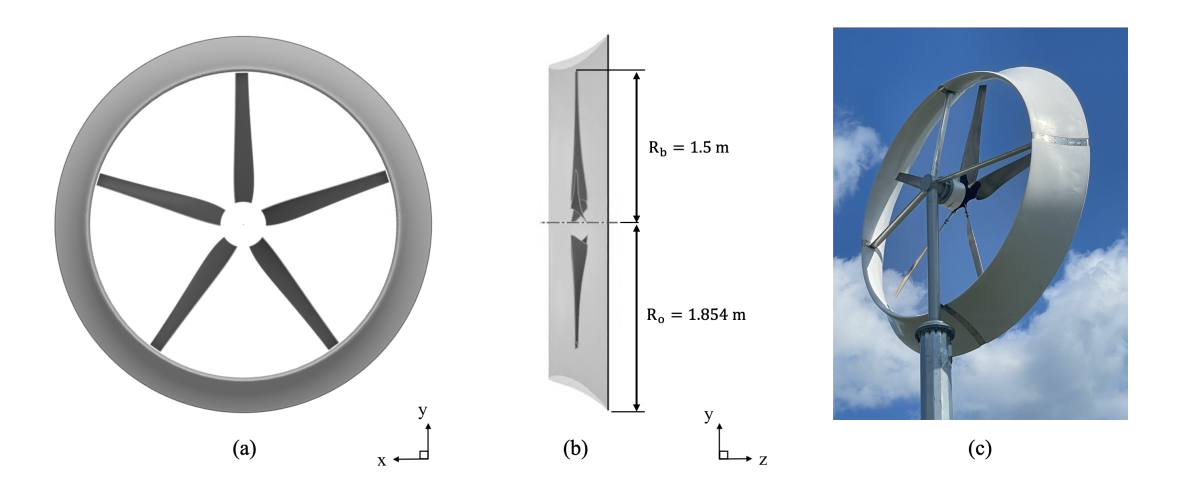


Figure 1. The DWT geometry features: (a) front view, (b) lateral view, and (c) photo of a real product

Table 1. DWT operating conditions

Parameter	Value			
Free Stream Velocity (V_0)	$6~\mathrm{m~s^{-1}}$			
Kinematic Velocity (ν)	$1.48 \times 10^{-5} \text{ m}^2 \text{ s}^{-1}$			
Tip Speed Ratio (λ)	2.9			
Rotation speed (Ω)	$11.6 \; {\rm rad \; s^{-1}}$			

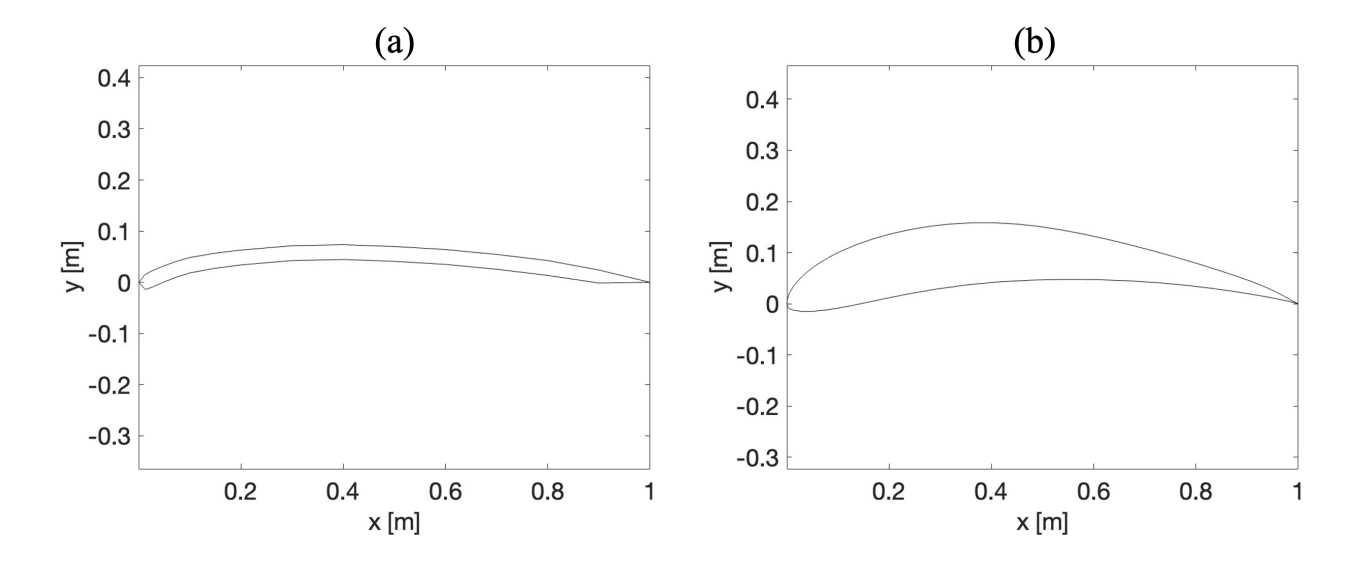


Figure 2. Geometry of the (a) GOE417a airfoil, (b) Eppler 423 airfoil





A cylindrical coordinate system (r, θ, z) was used to analyze the simulation results. The radial coordinate r measures the distance from the rotation axis, the azimuthal angle θ is defined counterclockwise from the x-axis shown in fig. 1, and the axial coordinate z corresponds to the streamwise direction, increasing downstream. The rotor was placed at z=0. The simulation was made nondimensional by the rotor radius (R), the freestream velocity (V_{∞}) , and the fluid density (ρ) . Inlet velocities were set by assigning a value of one to the axial (z-direction) velocity and zero to the other velocity components. To simulate the rotor rotation, the domain was rotated around the z-axis in the counterclockwise direction with a tip speed ratio $\lambda = \frac{R\Omega}{V_{\infty}}$ of 2.9. Since the flow behavior around each blade is identical, the domain only encompassed a fifth of the DWT geometry, as seen in fig. 3, and periodic boundary conditions were applied in θ . The inlet was located six rotor radii upstream of the rotor, and the outlet was located 12 radii downstream. The velocity was fixed at V_{∞} on the boundary at r=6R. This created a blockage ratio (the ratio of the duct cross-sectional area to the inlet cross-sectional area) of 4.2%. According to (Chen and Liou, 2011),

the calculated power coefficients (C_p) should be less than 5% higher than those calculated using an infinite domain.

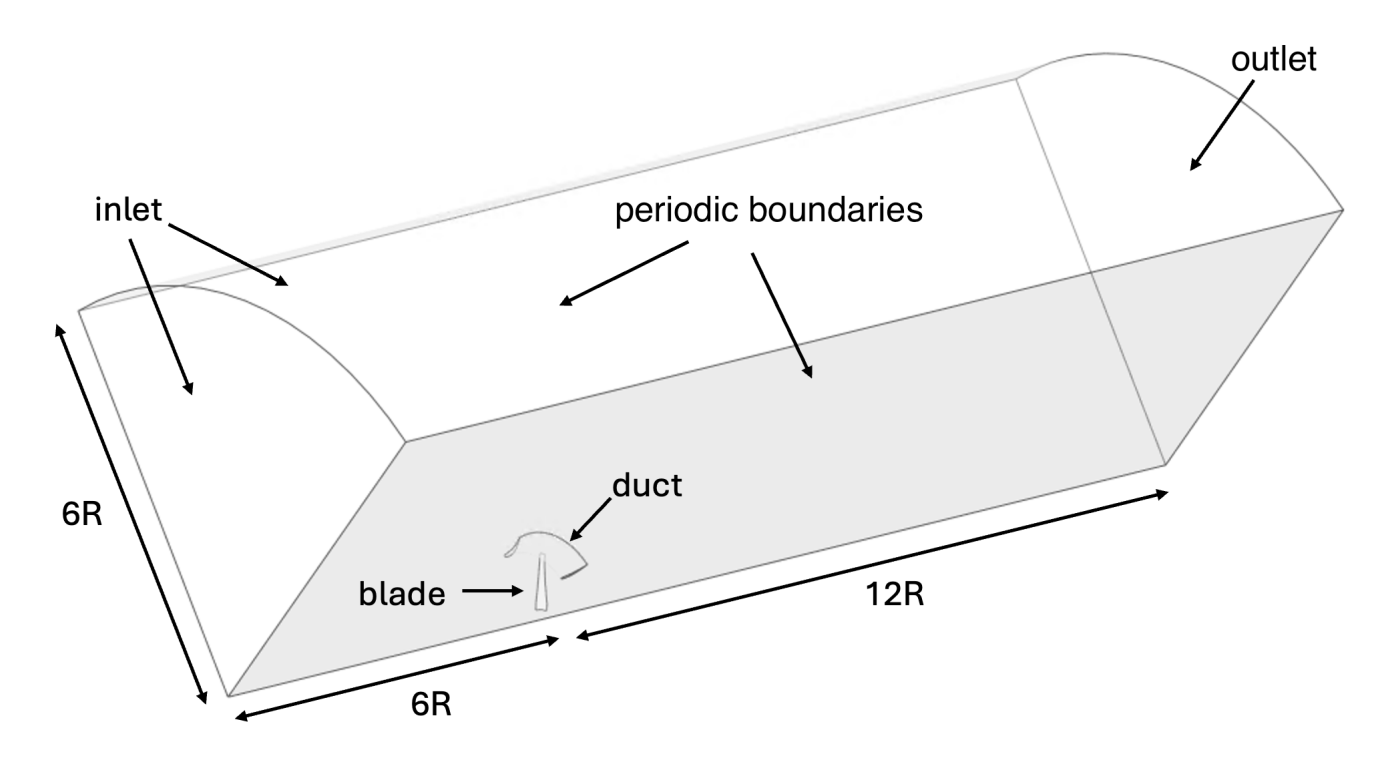


Figure 3. 3-D flow domain geometry

The $k-\epsilon$ turbulence model with enhanced wall treatment was chosen for the simulations. The calculations were performed in a rotating reference frame where the blades were stationary. Using this reference frame, steady-state simulations were run with the pressure-based solver and the coupled scheme used for the pressure-velocity coupling. Gradients were calculated using the least squares cell-based method, and second-order discretization schemes were used to calculate pressure, momentum, turbulent kinetic energy, and turbulent dissipation rate. At the inlet, the intensity and length scale of the turbulence were set





to 5% and 1 m, respectively (default setting). The outlet was set as a pressure outlet, and periodic boundary conditions were applied to the θ boundaries.

75 **2.2** Mesh

The meshing was performed using the Ansys meshing tool. The 3-D mesh was designed based on 2-D mesh convergence studies of the duct and blade airfoils (Tchapdieu, 2025), the results of which are summarized in table 2. The studies were performed under the conditions expected for the 3D simulations. In this table, estimated errors in the lift coefficient (calculated using Richardson extrapolation) are given as a function of the surface element size, E, and the first cell height of the boundary layer mesh, y_1 . y^+ values averaged over the airfoil surface, \bar{y}^+ , are also given.

Table 2. Grid refinement study of C_L for both airfoils

	GOE417a				E423				
Refinement level	E/c_{blade}	y_1/c_{blade}	% error C_L	\bar{y}^+	E/c_{duct}	y_1/c_{duct}	% error c_L	\bar{y}^+	
0	0.008	7.33×10^{-4}	1.6357	0.93	0.00150	3.73×10^{-5}	2.0339	0.98	
1	0.004	3.66×10^{-4}	1.0869	0.48	0.00080	1.86×10^{-5}	1.5351	0.49	
2	0.002	1.83×10^{-4}	0.2513	0.24	0.00038	9.32×10^{-6}	1.3293	0.25	
3	0.001	9.16×10^{-5}	0.0580	0.12	0.00019	4.66×10^{-6}	1.1485	0.12	

Based on these results, in 3-D face sizes with a respective element size of $E/c_{blade} = 0.09$ and $E/c_{duct} = 0.02$ and inflation layers with 15 layers, a growth rate of 1.2, and a first layer thickness of $y_1/c_{blade} = 1.10$ e-3 and $y_1/c_{duct} = 5.60$ e-5 were then applied on the blade and the duct surface. The mesh sizes were larger than the 2-D results to reduce computational cost and allow for mesh refinement. Mesh matching control was applied to the periodic boundaries. The resulting mesh is shown in Figure 4.

2.3 Numerical Validation

85

To assess the numerical accuracy, two refinements were performed on the initial mesh. Table 3 shows that refinement levels (RL) 0, 1, and 2 correspond to the mesh having approximately 1, 2.2, and 16 million nodes, respectively. The quantities used to assess the accuracy were the thrust (C_T) , power (C_P) , and total power $(C_{P_{total}})$ coefficients which are defined as

90
$$C_T = \frac{T}{\frac{1}{2}\rho V_\infty^2 A_{rotor}}$$
 (1)

$$C_P = \frac{P}{\frac{1}{2}\rho V_\infty^3 A_{rotor}} \tag{2}$$

$$C_{P_{total}} = \frac{P}{\frac{1}{2}\rho V_{\infty}^3 A_{duct}} \tag{3}$$





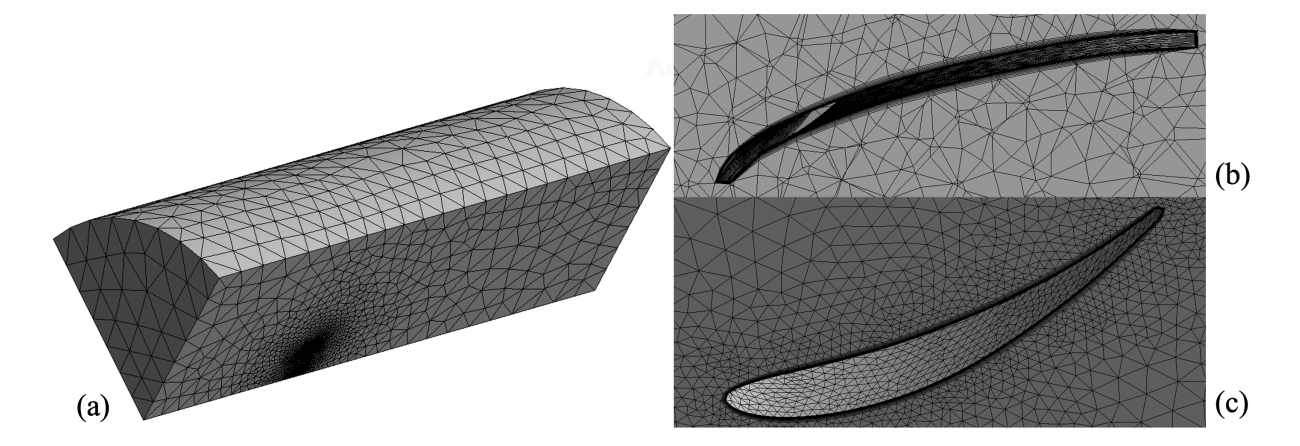


Figure 4. Mesh of the (a) domain, zoomed around (b) the blade section, and (c) the duct section

where T is the thrust applied to the rotor, P is the power produced, A_{rotor} is the area of the rotor, and A_{duct} is the exit area of the duct. C_P indicates the performance of a wind turbine relative to its rotor-swept area, while $C_{P_{total}}$ represents the performance relative to the exit area of the duct.

The thrust and torque generated by the rotor were directly computed using the Fluent z-direction force and moment calculator, respectively. The power produced by the DWT was computed using

$$100 \quad P = \tau \Omega \tag{4}$$

where τ is the torque generated by the turbine.

105

These quantities were computed at each refinement level (RL), as shown in columns 2–4 of Table 3. From RL 0 to 1, the percentage differences in the values of C_T and C_P were 3.5% and 6%, respectively. Increasing the RL from 1 to 2 reduced these differences to 0.09% and 1.14%, respectively. This decrease indicates good convergence of the simulation with respect to the grid size. Given the small percentage errors at RL 2, this mesh was considered sufficiently accurate, and all calculations presented in the subsequent sections were performed using the RL 2 mesh.

Table 3. Percentage error in values of interest after each refinement

		Bla	ade(GOE417a)		Duct(E423)					
RL	# nodes	E/c_{blade}	y_1/c_{blade}	\bar{y}^+	E/c_{duct}	y_1/c_{duct}	\bar{y}^+	C_T	C_P	$C_{P_{total}}$
0	1×10^6	0.090	1.10×10^{-3}	1.89	0.023	5.60×10^{-5}	1.21	0.9683	0.7242	0.4769
1	2.2×10^{6}	0.045	5.50×10^{-4}	1.02	0.011	2.80×10^{-5}	0.75	1.0017	0.7680	0.5058
2	16×10^6	0.023	2.75×10^{-4}	0.57	0.005	1.40×10^{-5}	0.48	1.0008	0.7767	0.5115





3 Actuator Disk Simulation Setup

The details of the actuator disk simulation setup for comparison with the 3-D simulations are presented in this section, including the geometry, meshing, and Fluent setup. No 2-D grid validation study was performed because the meshing closely followed the 3-D procedure.

3.1 Geometry & Fluent Setup

Figure 5 shows the axisymmetric actuator disk simulation domain. The simulation was nondimensionalized by the same parameters from the 3-D simulation. Inlet velocities were set by assigning a value of one to the axial (z-direction) velocity and zero to the other velocity component. The two flow domains have the same exact distances from the boundary conditions to the wind turbine. Therefore, the actuator disk simulation domain also had a blockage ratio of 4.2 %.

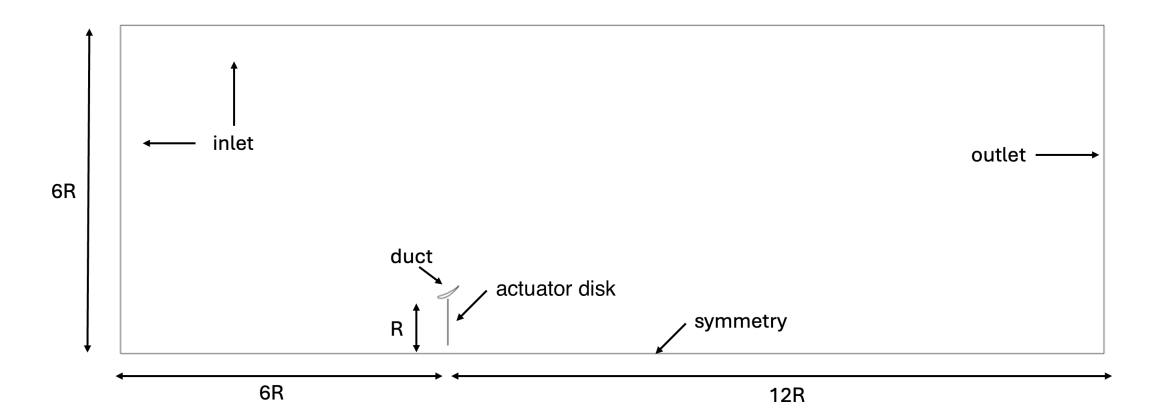


Figure 5. Actuator disk domain geometry

In the actuator disk simulation, the blades were replaced by a disk with a pressure drop given by

$$\delta p = \frac{T}{A_{rotor}},\tag{5}$$

where δp is the pressure drop across the disk and T is the thrust obtained from the 3-D blade resolved analysis. For the actuator-disk calculations, the power was calculated using

120
$$P = \delta p \iint v_{axial} dA_{rotor}.$$
 (6)

All additional settings were the same as used in the 3-D simulations.

3.2 Mesh

Meshing was again performed using the Ansys meshing tool following the same procedure used in 3-D. The mesh features of the E423 airfoil from RL 0 of the 2-D grid validation study (table 2) were applied to the duct. A face sizing was applied





to the actuator disk with an element size of $E/R = 5 \times 10^{-3}$. Lastly, an element size of E/R = 0.2 was applied to the whole domain. Figure 6 shows the baseline mesh of the actuator disk domain. The regions where the nondimensional pressure gradient exceeded 0.05 in the baseline mesh were then refined, and then a whole domain refinement was performed. Due to the low computational cost of this simulation technique and to ensure that the results were as accurate as possible, another domain refinement was performed to produce a final mesh for the actuator disk calculations having 200,000 nodes.

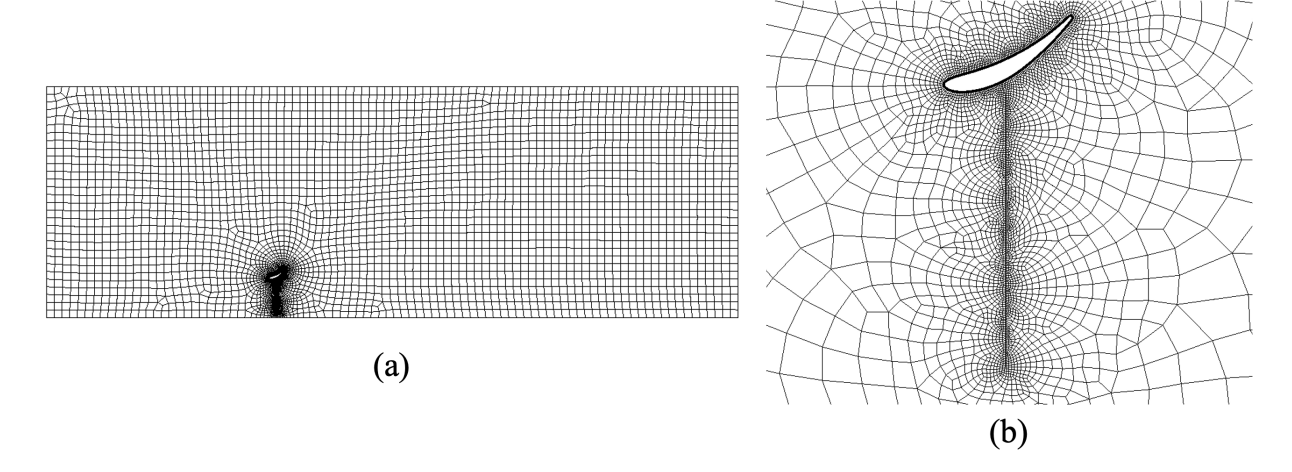


Figure 6. (a) Actuator disk mesh (b) zoomed region around actuator disk

130 4 Performance Comparison

135

140

The performance of the DWT, obtained from the two simulation approaches as a function of λ , is presented in fig. 7. The results of the 2-D and 3-D simulations are represented by dashed and solid curves, respectively. λ was varied by changing the rotational speed of the moving frame in the 3-D simulation. For each λ , the thrust calculated in 3-D was then used for a corresponding actuator disk simulation using the procedure described in section 3. Note that the blade design was not changed for different λ and therefore the DWT was off-design except at $\lambda = \lambda_{des} = 2.9$, the design point.

Figure 7 shows that the maximum C_P and $C_{P_{total}}$ for the 3-D simulation occurred at λ_{des} , as expected. The same behavior is seen for the 2-D simulation; however, the 2-D simulations predict a significantly higher maximum performance at λ_{des} . The performance predicted in 3-D were 26% lower than the 2-D calculations. This significant difference in performance predictions between the actuator disk and the blade-resolved simulation is possibly due to the fact that the actuator disk does not capture flow phenomena such as wake rotation and tip vortices, which will be investigated in the next section.

At tip speed ratios higher than the design value, the performance of the 3-D calculations tapers off, while the 2-D calculations remain fairly constant. This is a result of the fact that the 3-D thrust stays relatively constant under these conditions. As a reminder, the pressure drop used in the actuator disk model was based on the thrust generated by the DWT in the blade-resolved simulation, so as long as the thrust is the same, the 2-D performance will remain the same. The nearly constant thrust



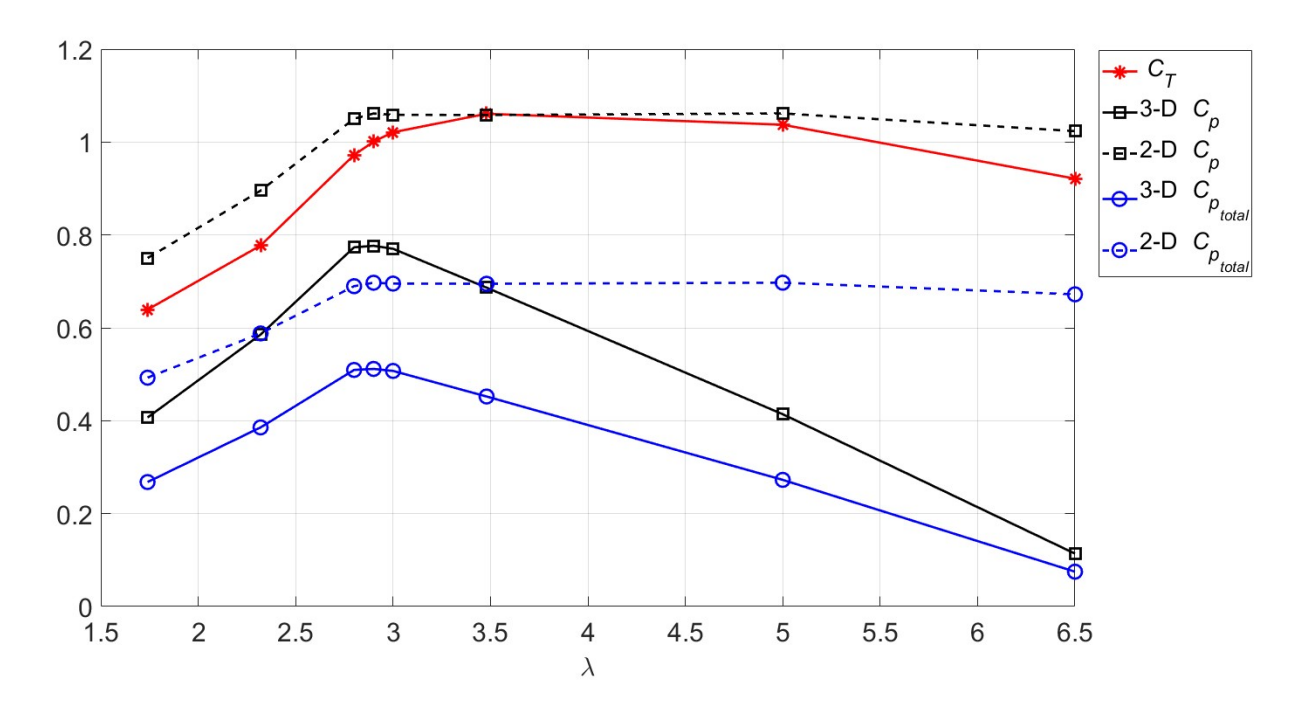


Figure 7. DWT Performance as a function of tip speed ratio calculated using 3-D blade-resolved simulations and 2-D actuator disk simulations

in 3-D is an outcome of the low value of λ_{des} for this device. For a device designed for a higher tip speed ratio, the thrust coefficient increases with λ for a wide range of tip speed ratios around the design tip speed ratio (Burton et al., 2011). Using a blade element analysis, it can be shown that the coefficient of thrust of a device designed for a lower tip speed ratio tends to have a maximum in the neighborhood of λ_{des} .

5 Flow Comparison

To compare the 2-D and 3-D flow features, the 3-D results were azimuthally averaged onto a Cartesian r-z grid in the domain $(z/R,r/R) \in [-1,2] \times [0,2]$. In both the r and z-directions, the spacing was 0.05 except in the intervals containing the duct where it was reduced to 0.01. If an r,z point corresponded to a θ curve that intersected the blade, the blade region was excluded from the average.

Figure 8(a) shows the azimuthally averaged axial velocity from the 3-D simulation, and Figure 8(b) shows the axial velocity from the 2-D simulation. In fig. 8(b) the actuator disk location is shown as a black dotted line. In both models, the magnitudes of the axial velocity of the flow increase as the duct is approached from the upstream. The highest axial velocity magnitudes are located near the tip and root of the blade/actuator disk, whereas the lowest axial velocity magnitudes are in the DWT wake





and above the duct. The shape of the shear layer that defines the radial bounds of the wake region is also similar. However, there are significant differences near the trailing edge of the duct.

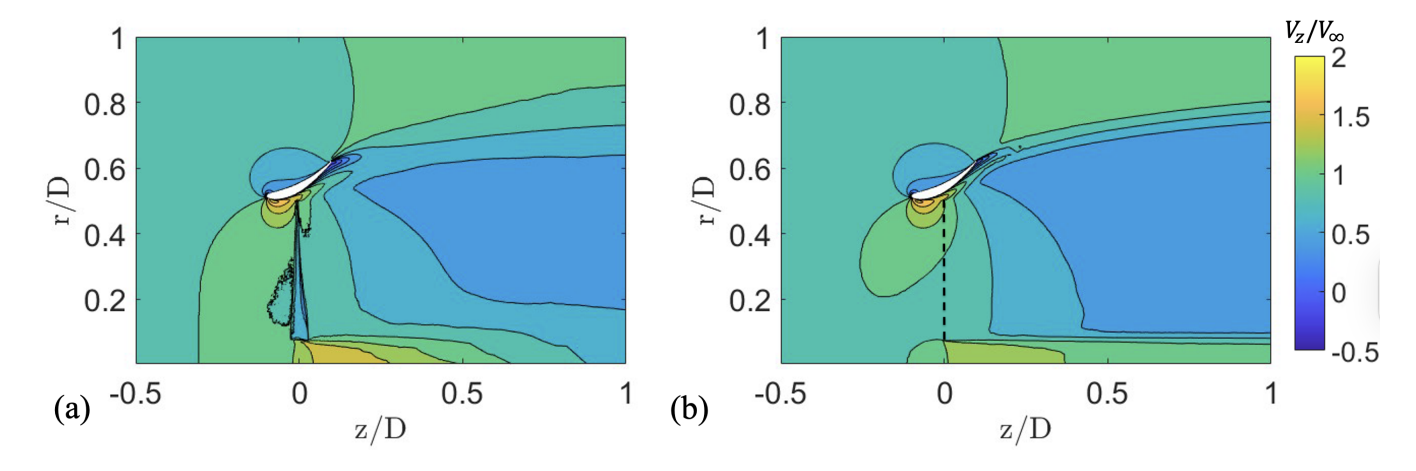


Figure 8. Axial velocity comparison between (a) 3-D blade-resolved simulation (b) 2-D actuator disk simulation

To investigate this, streamlines are plotted in Figure 9. In the 2-D simulation, there is no detectable separation, whereas in 3-D, there is a clear recirculation zone near the trailing edge of the duct which has a length of almost $c_{duct}/4$. The impact of this recirculation zone on wake expansion can be seen immediately downstream of the airfoil. In 2-D, the wake expands more, which is consistent with the 2-D case producing more power.

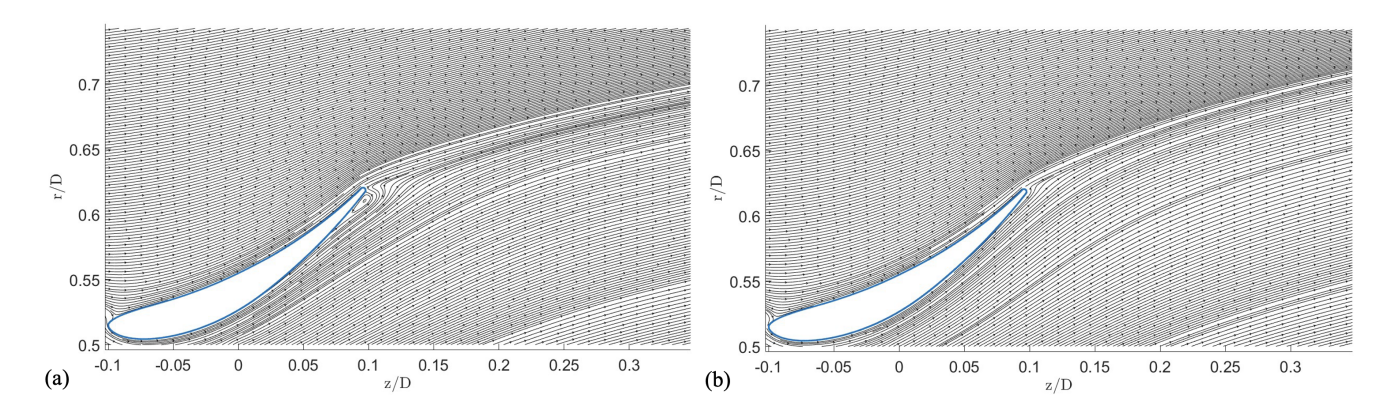


Figure 9. Streamline comparison between (a) 3-D blade-resolved simulation (b) 2-D actuator disk simulation

To provide a more quantitative view of the separation differences, the azimuthally averaged axial component of the 3-D skin friction on the inner surface of the duct was compared with its 2-D counterpart as shown in Figure 10. The axial skin friction coefficient on the duct goes to zero (indicating flow separation) at around Z/C = 0.75 in 3-D, as opposed to Z/C = 0.85 in 2-D. This 0.10 chord length difference indicates that separation occurs in both simulations but is more prevalent in 3-D.



170

175

180



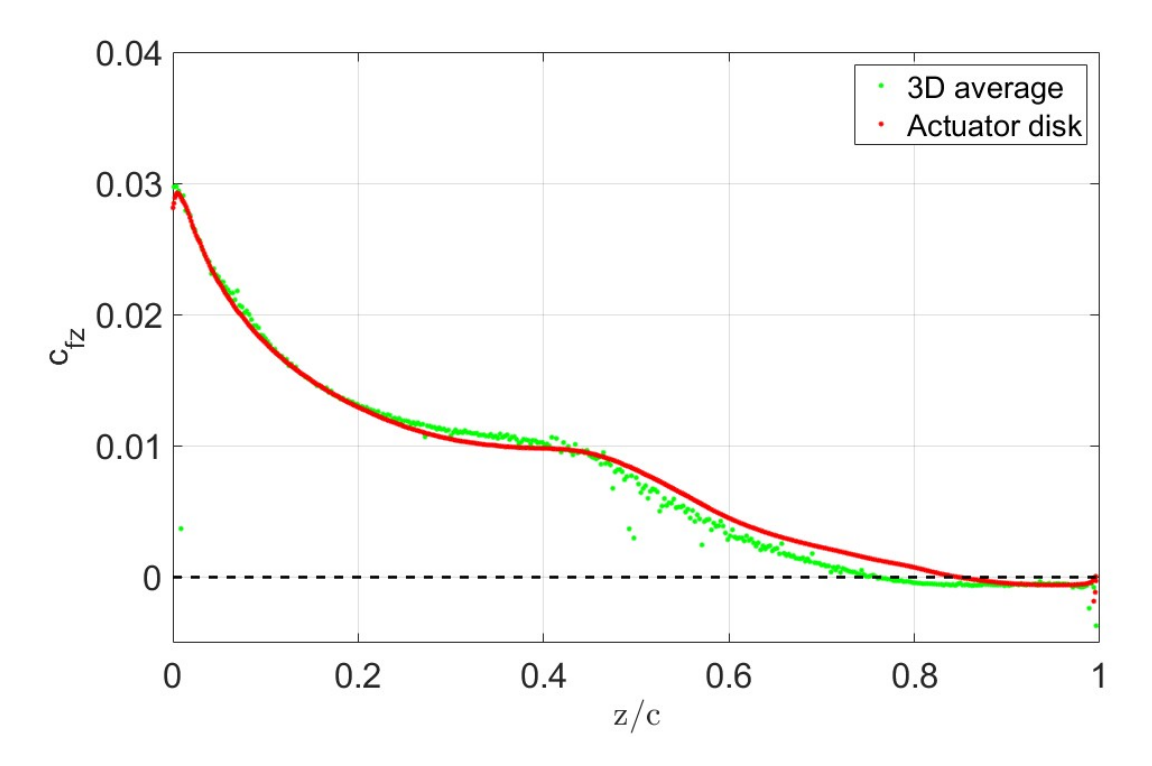


Figure 10. Axial skin friction coefficient comparison at the bottom part of the duct

One possible cause of the difference in separation position is the presence of swirl in the 3-D simulation. The swirl present in the wake of a wind turbine is caused by the rotation of the blade in the opposite direction. Figure 11 shows the azimuthally averaged swirl velocity from the 3-D simulation. (The 2-D simulation has no swirl velocity.) The swirl velocity has a magnitude of almost 80% of the freestream velocity near the root of the blades, indicating that it is a significant component of the flow velocity. Moving radially from the root, the swirl velocity decreases with the inverse of r in agreement with momentum theory (Glauert, 1983). Because swirl diminishes at the tips, it is not clear whether swirl is solely responsible for the increased separation in 3-D.

Another possible cause of the difference between the 2-D and 3-D simulations is that in the actuator disk simulation, the disk acts as a uniform resistance. In contrast, in the 3-D simulation, the blades are intermittent, and thus the flow may attach and separate as the blades pass. To understand this effect, Figure 12 shows the limiting streamlines (or equivalently skin friction lines (Delery, J., 2011)) on the inner surface of a fifth of the duct obtained from the 3-D simulation. The figure shows a flow separation curve where the limiting streamlines from the leading and trailing edges converge. The 3-D separation region is downstream of this curve. The 2-D separation region is the zone downstream of the dashed white line. This white line was obtained by determining the location where the value of c_{fz} goes to zero in Figure 10. Figure 12 is also colored by the axial skin friction coefficient. The curves defining the tip and root of the blade are shown in white, and the blade surface is gray.





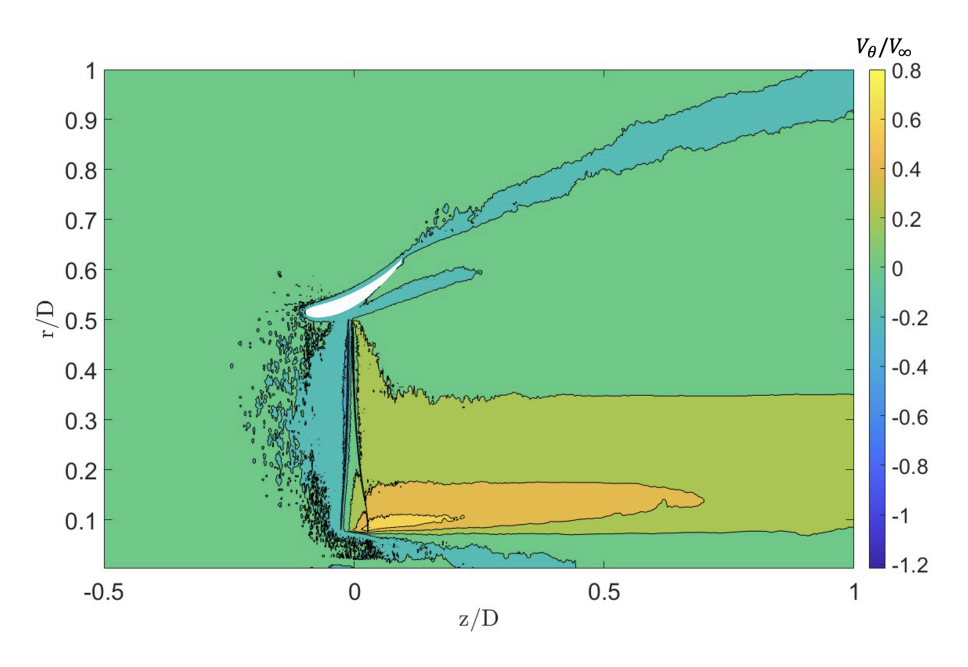


Figure 11. Azimuthally averaged swirl velocity contours

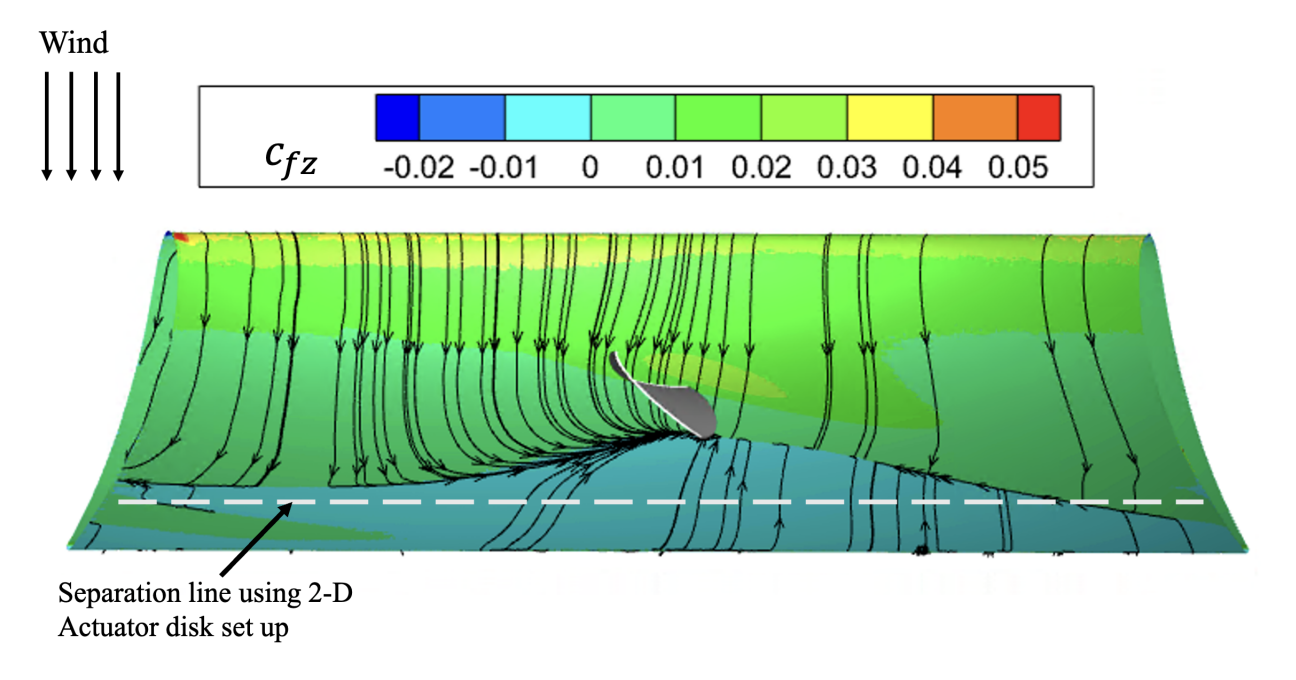


Figure 12. Limiting streamlines on the inner side of the duct colored by values of c_{fz} , rotor blade represented by gray surface

https://doi.org/10.5194/wes-2025-207
Preprint. Discussion started: 20 October 2025

© Author(s) 2025. CC BY 4.0 License.





Figure 12 illustrates that in the 3-D simulation, the separation zone is the largest near the rotor blade and decreases in size away from the blades. On the left side of the duct, the effect of the wake of the preceding blade can also be seen, where the flow separates and then reattaches. Thus, blade intermittency does have a strong effect on the separation. Compared to the 2-D separation zone (delineated by the white dashed line), the 3-D separation zone is almost always further upstream. Thus, blade intermittency not only causes an oscillation in the separation location but may also be responsible for a shift in the mean separation location. It is surmised that with a larger blade count and the same loading, the 3-D results would be closer to the actuator disc simulations.

190 6 Conclusions

195

200

205

The flow around a ducted wind turbine designed using a 2-D actuator disk simulation was simulated using a RANS 3-D blade-resolved simulation and a 2-D actuator-disk simulation. The performance predicted by the 3-D blade resolved simulation was 26 % less than that predicted by the 2-D actuator disk simulations. The flow features between the two simulation methods agreed qualitatively, but flow separation started earlier in the 3-D simulation. A recirculation zone was found near the trailing edge of the duct in the blade-resolved simulation, while it was almost nonexistent in the actuator disk simulation. It can postulated that a lower duct angle attack compared to the one obtained from the 2-D optimization could be beneficial to the overall performance of a finite bladed DWT as it would reduce the amount of separation that occurs.

A large part of the possible differences between the two simulation methods could be attributed to the absence of a swirl velocity in the actuator disk simulation. In future work, a swirl velocity will be introduced to the actuator disk simulation to potentially mitigate its differences from the blade-resolved simulation.

Code and data availability. All data and MATLAB code can be provided by the corresponding author upon request.

Author contributions. The overall research was conceptualized by Junior Tchapdieu, Brian Helenbrook, and Kenneth Visser. Junior Tchapdieu developed the methodology, implemented the necessary models, conducted the formal analysis, collected and curated the data, and was responsible for software development and validation of results. He also prepared the original draft of the manuscript. Brian Helenbrook and Kenneth Visser provided supervision throughout the project, contributed to the development of the methodology, and were actively involved in the critical review and editing of the manuscript. All authors contributed to the visualization and interpretation of the results and approved the final version of the manuscript.

Competing interests. The authors declare that they have no conflict of interest.





References

- Abe, K.-i., and Ohya, Y.: An investigation of flow fields around flanged diffusers using CFD, Journal of wind engineering and industrial aerodynamics, Vol. 92, No. 3-4, pp. 315–330, https://doi.org/10.1016/j.jweia.2003.12.003, 2004.
 - Aranake, A., and Duraisamy, K.: Aerodynamic optimization of shrouded wind turbines, Wind Energy, Vol. 20, No. 5, pp. 877–889, https://doi.org/10.1002/we.2068, , 2017.
- Aranake, A. C., Lakshminarayan, V. K., and Duraisamy, K.: Computational analysis of shrouded wind turbine configurations using a 3-dimensional RANS solver, Renewable Energy, Vol. 75, pp. 818–832, https://doi.org/10.1016/j.renene.2014.10.049, 2015.
 - Bagheri-Sadeghi, N., Helenbrook, B. T., and Visser, K. D.: Ducted wind turbine optimization and sensitivity to rotor position, Wind Energy Science, Vol. 3, No. 1, pp. 221–229, https://doi.org/10.5194/wes-3-221-2018, 2018.
 - Bagheri-Sadeghi, N., Helenbrook, B. T., and Visser, K. D.: Maximal power per device area of a ducted turbine, Wind Energy Science, Vol. 6, No. 4, pp. 1031–1041, https://doi.org/10.5194/wes-6-1031-2021, 2021.
- Belloni, C., Willden, R., and Houlsby, G.: An investigation of ducted and open-centre tidal turbines employing CFD-embedded BEM, Renewable Energy, Vol. 108, pp. 622–634, https://doi.org/10.1016/j.renene.2016.10.048, 2017.
 - Bontempo, R., Manna, M.: Performance analysis of open and ducted wind turbines, Applied Energy, Vol. 136, pp. 405-416, https://doi.org/10.1016/j.apenergy.2014.09.036, 2014.
 - Burton, T., Jenkins, N., Sharpe, D., and Bossanyi, E.: Wind energy handbook" John Wiley & Sons, ISBN: 978-0-470-69975-1, 2011.
- Chen, T., and Liou, L.: Blockage corrections in wind tunnel tests of small horizontal-axis wind turbines, Experimental Thermal and Fluid Science, Vol. 35, No. 3, pp. 565–569, https://doi.org/10.1016/j.expthermflusci.2010.12.005, 2011.
 - Cresswell, N., Ingram, G., and Dominy, R.: The impact of diffuser augmentation on a tidal stream turbine, Ocean Engineering, Vol. 108, pp. 155–163, https://doi.org/10.1016/j.oceaneng.2015.07.033, 2015.
- Delery, J.: Separation in three-dimensional flow: critical points, separation lines and vortices, ONERA Information Resources. ONERA, 230 2011.
 - Dick, E.: Power limits for wind energy concentrator systems, Wind Engineering, 1986, pp. 98-115.
 - Ding, C., Zhang, B., Liang, C., Visser, K., and Yao, G.: High-Order Large Eddy Simulations of a Wind Turbine in Ducted and Open-Rotor Configurations, Journal of Fluids Engineering, Vol. 145, No. 2, p. 021201, https://doi.org/10.1115/1.4055989, 2023.
- Dubief, Y., and Delcayre, F.: On coherent-vortex identification in turbulence, Journal of turbulence, Vol. 1, No. 1, p. 011, https://doi.org/10.1088/1468-5248/1/1/011, 2011.
 - Ducted Wind Turbine, I.: D3 Turbine, https://www.ductedwind.com/technology/commercial-specifications, 2019. Accessed: 2024-11-26.
 - Feng, B., Liu, X., Ying, Y., Si, Y., Zhang, D., and Qian, P.: Research on the tandem arrangement of the ducted horizontal-axis tidal turbine, Energy Conversion and Management, Vol. 258, p. 115546, https://doi.org/10.1016/j.enconman.2022.115546, 2022.
- Foote, T., and Agarwal, R.: Optimization of power generation from shrouded wind turbines, International Journal of Energy and Environment (Print), Vol. 4, https://doi.org/10.1115/ES2012-91005, 2013.
 - Ghenai, C., Salameh, T., and Janajreh, I.: Modeling and Simulation of Shrouded Horizontal Axis Wind Turbine Using RANS Method, Jordan Journal of Mechanical & Industrial Engineering, Vol. 11, No. 4, 2017
 - Gilbert, B. L., and Foreman, K. M.: Experimental demonstration of the diffuser-augmented wind turbine concept, Journal of Energy, Vol. 3, No. 4, pp. 235–240, https://doi.org/10.2514/3.48002, 1979.
- 245 Gilbert, B., and Foreman, K.: Experiments with a diffuser-augmented model wind turbine, https://doi.org/10.1115/1.3230875, 1983.



265



- Gilbert, B. L., Oman, R. A., and Foreman, K. M.: Fluid dynamics of diffuser-augmented wind turbines, Journal of Energy, Vol. 2, No. 6, pp. 368–374, https://doi.org/10.2514/3.47988, 1978.
- Glauert, H.: The elements of aerofoil and airscrew theory Cambridge university press, ISBN: 052127494, 1983.
- Hansen, M.: Aerodynamics of wind turbines, Routledge, ISBN: 978-1-138-77507-7, 2015.
- Hansen, M. O. L., Sørensen, N. N., and Flay, R.: Effect of placing a diffuser around a wind turbine, Wind Energy: An International Journal for Progress and Applications in Wind Power Conversion Technology, Vol. 3, No. 4, https://doi.org/10.1002/we.37, 2000, pp. 207–213.
 - Jafari, S. A., and Kosasih, B.: Flow analysis of shrouded small wind turbine with a simple frustum diffuser with computational fluid dynamics simulations, Journal of Wind Engineering and Industrial Aerodynamics, Vol. 125, pp.102–110, https://doi.org/10.1016/j.jweia.2013.12.001, 2014.
- Jamieson, P.: Beating betz-energy extraction limits in a uniform flow field, European Wind Energy Conference (EWEC), Brussels, Belgium, Mar, 2008, pp. 1–10.
 - Jamieson, P.: Generalized limits for energy extraction in a linear constant velocity flow field, Wind Energy: An International Journal for Progress and Applications in Wind Power Conversion Technology, Vol. 11, No. 5, pp. 445–457, https://doi.org/10.1002/we.268, 2008.
 - Jamieson, P. M.: Beating betz: energy extraction limits in a constrained flow field, https://doi.org/10.1115/1.3139143, 2009.
- 260 Jamieson, P.: Innovation in wind turbine design, John Wiley & Sons, ISBN:9780470699812, 2018.
 - Kanya, B. and Visser, K. D.: Experimental Validation of a Ducted Wind Turbine Design Strategy, Wind Energ. Sci., 3, 919-928, https://doi.org/10.5194/wes-3-919-2018, 2018.
 - Kogan, A., Nissim, E., and Seginer, A.: Shrouded aerogenerator design study, Technion Research and Development Foundation, 1961.
 - Liu, Y., and Yoshida, S.: An extension of the Generalized Actuator Disc Theory for aerodynamic analysis of the diffuser-augmented wind turbines, Energy, Vol. 93, 2015, pp. 1852–1859.
 - Moeller, M., and Visser, K.: Experimental and numerical studies of a high solidity, low tip speed ratio DAWT, 48th AIAA aerospace sciences meeting including the new horizons forum and aerospace exposition, p. 1585, https://doi.org/10.2514/6.2010-1585, 2010.
 - Ohya, Y., and Karasudani, T.: A shrouded wind turbine generating high output power with wind-lens technology, Energies, Vol. 3, No. 4, 2010, pp. 634–649, https://doi.org/10.3390/en3040634, 2010.
- Ohya, Y., Karasudani, T., Sakurai, A., Abe, K.-i., and Inoue, M.: Development of a shrouded wind turbine with a flanged diffuser, Journal of wind engineering and industrial aerodynamics, Vol. 96, No. 5, pp. 524–539, https://doi.org/10.1016/j.jweia.2008.01.006, 2008.
 - Rahmatian, M. A., Tari, P. H., Mojaddam, M., and Majidi, S.: Numerical and experimental study of the ducted diffuser effect on improving the aerodynamic performance of a micro horizontal axis wind turbine, Energy, Vol. 245, p. 123267, https://doi.org/10.1016/j.energy.2022.123267, 2022.
- Roshan, S. Z., Alimirzazadeh, S., and Rad, M.: RANS simulations of the stepped duct effect on the performance of ducted wind turbine, Journal of Wind Engineering and Industrial Aerodynamics, Vol. 145, pp. 270–279, https://doi.org/10.1016/j.jweia.2015.07.010, 2015.
 - Sajadmanesh, S. M., Mohseni, A., and Mojaddam, M.: Vortex dynamics mechanisms of separated boundary layer in a highly loaded low pressure turbine cascade, International Journal of Heat and Fluid Flow, Vol. 82, p. 108540, https://doi.org/10.1016/j.ijheatfluidflow.2020.108540, 2020.
- Schmitz, F.W.: Aerodynamics of the Model Airplane. Part 1. Airfoil Measurements RISC-721, Translation Branch Redstone Scientific Information Center, 1967. (Original German 1942).
 - Selig, M. S., Lyon, C. A., Giguere, P., Ninham, C. P., and Guglielmo, J. J.: Summary of Low-Speed Airfoil Data, Vol. 2, Tech. rep., UIUC, Virginia Beach, Virginia, 1996.

https://doi.org/10.5194/wes-2025-207 Preprint. Discussion started: 20 October 2025 © Author(s) 2025. CC BY 4.0 License.



295



- Shive, M., and Crawford, C.: Ducted turbine blade optimization using numerical simulation, ISOPE International Ocean and Polar Engineering Conference, ISOPE, 2011, pp. ISOPE–I.
 - Sobieczky, H.: Parametric airfoils and wings, Recent development of aerodynamic design methodologies: inverse design and optimization, Springer, 1999, pp. 71–87.
 - Tchapdieu, J. E.: Ducted Wind Turbine Flow Features Comparison Using Blade Resolved And Actuator Disk Simulation, M.S. thesis, Clarkson University, 2025
- Van Bussel, G. J. W.: The science of making more torque from wind: Diffuser experiments and theory revisited. Journal of Physics: Conference Series, Vol. 75, IOP Publishing, p. 012010, https://doi.org/10.1088/1742-6596/75/1/012010, 2007.
 - Venters, R., Helenbrook, B. T., and Visser, K. D.: Ducted wind turbine optimization, Journal of Solar Energy Engineering, Vol. 140, No. 1, p.011005, https://doi.org/10.1115/1.4037741, 2018.
 - Visser, K. D.: "Real-world development challenges of the Clarkson University 3 meter ducted wind turbine", J. Phys.: Conf. Ser. 2265 042072, TORQUE 2022, Delft, The Netherlands, https://doi.org/10.1088/1742-6596/2265/4/042072, June 2022.
 - Wang, S.-H., and Chen, S.-H.: Blade number effect for a ducted wind turbine, Journal of mechanical science and technology, Vol. 22, pp. 1984–1992, https://doi.org/10.1007/s12206-008-0743-8, 2008.